



## Effects of Co doping on the structure and physicochemical properties of hausmannite (Mn<sub>3</sub>O<sub>4</sub>) and its transformation during aging

Shuang Zhang<sup>a,b</sup>, Hui Li<sup>c</sup>, Zhongkuan Wu<sup>d</sup>, Jeffrey E. Post<sup>e</sup>, Bruno Lanson<sup>f</sup>, Evert J. Elzinga<sup>g</sup>, Yurong Liu<sup>a,b</sup>, Haigang Li<sup>h</sup>, Mei Hong<sup>h</sup>, Fan Liu<sup>a,b</sup>, Hui Yin<sup>a,b,\*</sup>

<sup>a</sup> Key Laboratory of Arable Land Conservation (Middle and Lower Reaches of Yangtse River), Ministry of Agriculture and Rural affairs, College of Resources and Environment, Huazhong Agricultural University, Wuhan 430070, China

<sup>b</sup> State Environmental Protection Key Laboratory of Soil Health and Green Remediation, Ministry of Ecology and Environment, Huazhong Agricultural University, Wuhan 430070, China

<sup>c</sup> Environmental Sciences Division, Oak Ridge National Laboratory, Oak Ridge, TN 37831, United States of America

<sup>d</sup> College of Environment, Zhejiang University of Technology, Hangzhou 310014, China

<sup>e</sup> Department of Mineral Sciences, NHB 119, Smithsonian Institution, Washington, DC 20013-7012, USA

<sup>f</sup> Univ. Grenoble Alpes, Univ. Savoie Mont Blanc, CNRS, IRD, Univ. Gustave Eiffel, ISTerre, F-38000 Grenoble, France

<sup>g</sup> Department of Earth and Environmental Sciences, Rutgers University, Newark, NJ 07102, United States

<sup>h</sup> College of Grassland, Resources and Environment, Inner Mongolia Agricultural University, Hohhot 010018, China

### ARTICLE INFO

Editor: Hailiang Dong

#### Keywords:

Mn oxide  
Hausmannite  
Transition metal  
Cobalt  
Transformation

### ABSTRACT

Hausmannite is a common low-valence manganese oxide mineral with a distorted spinel structure in surficial sediments. Although natural Mn oxides often contain various transition metal (TM) impurities, few studies have addressed the substitution mechanisms of TMs, such as cobalt (Co), with hausmannite and induced changes in the mineral physicochemical properties. In this study, Co-doped hausmannites with final Co/Mn molar ratios of 0.05 and 0.11 were synthesized and characterized by wet chemical analysis, powder X-ray diffraction (XRD), Fourier transformed infrared spectra (FTIR), high resolution transmission electron microscope (HRTEM), X-ray photoelectron spectroscopy (XPS) and X-ray absorption fine structure spectroscopy (XAFS). Co-doped samples have larger crystallite sizes and smaller specific surface areas than those of the hausmannite without Co. The Co cations exist in a mixed-valence of +3 and +2. Powder XRD and acid dissolution experiments indicate that Co incorporates into the mineral structures, and increases the mineral structural stability. Co K-edge extended X-ray adsorption fine structure (EXAFS) analysis demonstrates that Co likely substitutes for lattice Mn(III). After aging at room temperature for three years, 14.1 ± 1.9% of pure hausmannite is transformed to manganite while only 2.6 ± 0.7% of manganite appears in the aged Co-doped sample with an initial Co/Mn molar ratio of 0.10. These results provide new insights into the incorporation mechanisms of TMs into low valence Mn oxides, and the stability of these minerals in natural environments.

### 1. Introduction

Manganese (Mn) oxide minerals in various geological settings are often enriched in various transition metals (TMs). Incorporation of TMs into Mn oxides can modify the mineral substructure, physicochemical properties and reactivity towards various pollutants (Song et al., 2020; Yin et al., 2012). Our previous studies on the effects of TMs on the reactivity of hexagonal birnessite towards various pollutants convincingly demonstrate that the reactivity of these TM-containing minerals,

which are close to natural analogs, can be much different from those of the pure one. For example, incorporation of Ni into hexagonal birnessite greatly reduces the adsorption densities of heavy metals, Pb<sup>2+</sup> or Zn<sup>2+</sup>, on the minerals by 79–85% (Yin et al., 2012). The removal efficiencies of Cr<sup>3+</sup> from water by Co- and Ni-containing birnessites are 28–55% and 67–78%, respectively, that of the pure birnessite (Yin et al., 2020a).

Hausmannite is not only the fifth most common Mn oxide mineral in soils and sediments, but is also found in hydrothermal and metamorphic deposits (Chartier et al., 1999; Giovannelli et al., 2012; Jarosch, 1987).

\* Corresponding author at: Key Laboratory of Arable Land Conservation (Middle and Lower Reaches of Yangtse River), Ministry of Agriculture and Rural affairs, College of Resources and Environment, Huazhong Agricultural University, Wuhan 430070, China.

E-mail address: [yinhui666@mail.hzau.edu.cn](mailto:yinhui666@mail.hzau.edu.cn) (H. Yin).

<https://doi.org/10.1016/j.chemgeo.2021.120448>

Received 13 April 2021; Received in revised form 16 June 2021; Accepted 19 July 2021

Available online 21 July 2021

0009-2541/© 2021 Elsevier B.V. All rights reserved.

It has a tetragonally deformed spinel structure, elongated along the *c* axis, with  $\text{Mn}^{2+}$  occupying the tetrahedral sites and Jahn-Teller active  $\text{Mn}^{3+}$  in the octahedral sites (Bordeneuve et al., 2010; Jarosch, 1987; Sukhdev et al., 2020). Hausmannite is usually not only the precursor or secondary product of other Mn oxide phases (Barreto et al., 2020; Birkner and Navrotsky, 2012; Birkner and Navrotsky, 2014; Feng et al., 2004), but also can have adsorption and redox reactivity towards a variety of metal pollutants (Barreto et al., 2020; Johnson et al., 2018; Shaughnessy et al., 2003; Song et al., 2020; Wilk et al., 2005).

Being the most widely distributed Mn oxide spinel, hausmannite is capable of housing various substituents, including Co, Ni, Fe and Al (Antao et al., 2019; Baron et al., 1998; Bordeneuve et al., 2010; Green et al., 2004; Lefkowitz and Elzinga, 2015; Rajeesh Kumar et al., 2021; Song et al., 2020). Substitution of  $\text{Fe}^{3+}$  for  $\text{Mn}^{3+}$  into the octahedral site in hausmannite decreases the Jahn-Teller distortion, increases the Curie point, and decreases the spontaneous magnetization (Baron et al., 1998). Zn doping changes the morphologies of the obtained hausmannite crystallites from nanorods for the pure mineral to a mixture of nanorods and nanoparticles, and increases the energy bandgap (Jha et al., 2012). Pb doping greatly reduces the  $\text{Mn}_3\text{O}_4$  particle size and increases the bandgap, dielectric constant, and AC conductivity (Şahin et al., 2020). Doping with various TMs ( $\text{Cr}^{3+}$ ,  $\text{Co}^{2+}$ ,  $\text{Ni}^{2+}$ , and  $\text{Cu}^{2+}$ ) greatly enhances the phase stability during cycling and charge-transfer behaviors of hausmannite (Dong et al., 2013). However, these studies mainly focus on the applications of TM-modified hausmannites in materials sciences. It is recently reported that Ni substitution in hausmannite causes noticeable changes in the mineral structure (e.g. lattice parameters), and enhances mineral acid dissolution and oxidation reactivity towards As(III) at pH = 5 (Song et al., 2020). This indicates that structural impurities may modify the structure and physicochemical properties of hausmannite and thus the adsorption and redox reactivity towards pollutants. Unlike Ni, Co is highly redox-sensitive, and the influence of Co incorporation on the reactivity and stability of hausmannite remains to be determined.

Further, as a kind of metastable mineral, hausmannite can be converted into other Mn oxides phases during aging. These processes can be affected by mineral properties, such as chemical composition and particle sizes, and environmental conditions, e.g., moisture, temperature and  $\text{O}_2$  (Birkner and Navrotsky, 2012; Birkner and Navrotsky, 2014; Kirillov et al., 2009; Rabiei et al., 2005). At 60% relative humidity at room temperature, hausmannite can change its morphology and chemical identity to manganite (Rabiei et al., 2005). Upon slow oxidation at room temperature for 1 year, the hausmannite content in a mixture of hausmannite with manganite is decreased from 47% to 28% (Kirillov et al., 2009). Small crystallite size is reported to promote hausmannite transformation (Birkner and Navrotsky, 2012; Birkner and Navrotsky, 2014). These previous studies mainly focus on the aging of pure hausmannite. However, the effect of TM doping on the stability of hausmannite and its transformation during aging remains largely unexplored.

The present work aims to investigate the effect of Co doping on the mineral structure, physicochemical properties and stability during aging at room temperature. Specifically, Co-doped hausmannite samples were synthesized at room temperature by a coprecipitation method, and characterized by powder XRD, FTIR and HRTEM. The valence and crystal chemistry of Mn and Co were investigated by XPS, Co K-edge XAFS and acid dissolution experiments. These findings will help in understanding the effects of TM doping on the structure, properties and stability of low valence Mn oxide minerals in natural environments.

## 2. Materials and methods

### 2.1. Preparation of Co-doped hausmannites

Cobalt substituted hausmannite was prepared according to the method described in (Giovannelli et al., 2012). In detail,  $\text{CoSO}_4 \cdot 7\text{H}_2\text{O}$

was added to 200 mL of 0.5 M  $\text{MnSO}_4$  solution to obtain an initial Co/Mn molar ratio of 0, 0.05 and 0.10. After the solution was uniformly mixed, 2 M NaOH solution was added dropwise to keep the suspension pH above 10 for 6 h under stirring in air at room temperature. The pH was recorded by a pH-meter. At the end of the reaction, the slurry was filtered, rinsed with deionized water until the conductivity of filtrate was  $<20 \mu\text{s cm}^{-1}$  to eliminate the salt excess, and dried at  $40^\circ\text{C}$  for 3 days, and then ground and sieved (100 mesh). The prepared samples were designated as HM, CoH5, and CoH10 correspondingly.

Portions of the HM and CoH10 powders were stored in closed tubes at room temperature ( $25 \pm 5^\circ\text{C}$ ) under air condition in the laboratory for three years, and the humidity in laboratory around 50%. The corresponding samples were named as agedHM and agedCoH10.

### 2.2. Sample characterization

The phase purity of prepared samples was analyzed using a Bruker D8 Advance diffractometer with Cu K $\alpha$  radiation ( $\lambda = 0.15418 \text{ nm}$ ). The diffractometer was operated at a tube voltage of 40 kV and a tube current of 40 mA in the range of  $2\theta$  of  $5\text{--}85^\circ$  at a step of  $0.02^\circ$  and an integration time of 1.2 s. Rietveld structure refinements were performed using software TOPAS (version 4.2). The specific surface areas (SSA) were measured by  $\text{N}_2$  adsorption at liquid nitrogen temperature (77 K) with an Autosorb-1 standard physical adsorption analyzer (Quantachrome Autosorb-1, USA). The samples (100 mg) were degassed under vacuum at  $110^\circ\text{C}$  for 3 h before  $\text{N}_2$  adsorption, and SSA was calculated by employing the multi-point BET method. HRTEM analysis and selected-area electron diffraction were employed to obtain mineral morphologies, particle sizes, and phase lattice on a JEM-2100F (JEOL, Japan) at 200 keV. The samples were prepared by adding 50  $\mu\text{L}$  of 0.1  $\text{g}\cdot\text{L}^{-1}$  mineral suspension onto a 200-mesh carbon-coated copper grid (Beijing Zhongjingkeyi Technology Co., Ltd.), and dried at room temperature under air condition. FTIR analyses were performed on a Bruker Equinox 55 model spectrophotometer using KBr pellets with a spectral range of  $4000\text{--}400 \text{ cm}^{-1}$ . XPS of Mn 2p and Co 2p were measured on a VG Multilab 2000 X-ray photoelectron spectrometer with a Mg K $\alpha$  X-ray source (1253.6 eV) using the large area mode with a pass energy of 25 eV and an energy step size of 0.1 eV. Adventitious C 1 s binding energy was used to calibrate the energy and set to 284.8 eV. Data were analyzed using Avantage software, and a Shirley background was used (Yin et al., 2011). For Mn 2p fitting, the fit parameters were used from a previous study (Ilton et al., 2016).

The sample chemical composition was determined via atomic absorption spectrometry (AAS, Varian AAS 240FS) after dissolving 0.1000 g solid in a mixture of 25 mL of 0.25 M  $\text{NH}_2\text{OH}\cdot\text{HCl}$  solution and 1 M  $\text{H}_2\text{SO}_4$  solution. Triplicate analyses were performed. Method blanks and matrix spikes were also analyzed along with samples for quality assurance and quality controls, and the spiked recoveries of  $\text{Mn}^{2+}$  were between 98 and 102% (mean recovery:  $100 \pm 2\%$ ).

### 2.3. Dissolution experiments

The acid dissolution experiment was performed by adopting the method in our previous study (Qin et al., 2017). Briefly, 0.10 g sample was added into 250 mL of 2 M HCl solution while stirring at a constant rate with a magnetic stir at room temperature. At predetermined time intervals, an aliquot of 5 mL suspension was taken out and immediately filtered through 0.22  $\mu\text{m}$  membrane (Shanghai Xingya purification material factory). The concentration of  $\text{Mn}^{2+}$  and  $\text{Co}^{2+}$  in the filtrate were analyzed using AAS. The metal (Me) dissolution ratio was calculated as  $\chi_{\text{Me}} = \text{Me}(t)/\text{Me}(\text{total})$ , where Me (t) is the concentration of metal in solutions at time t, and Me(total) is the final metal concentration after complete dissolution of the mineral.

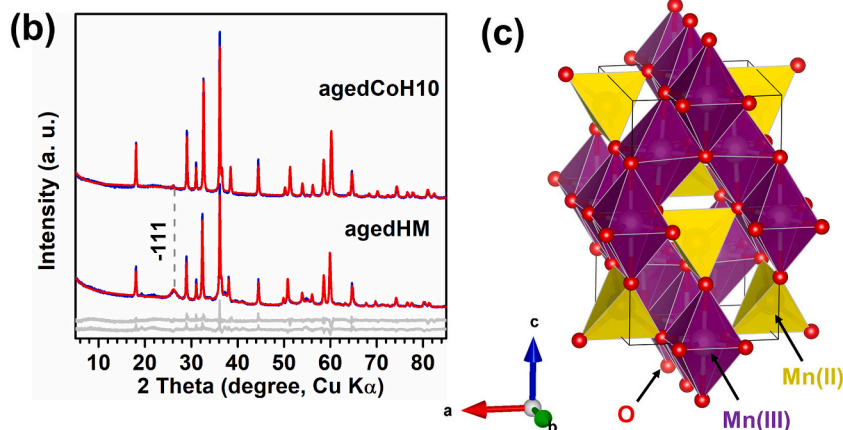
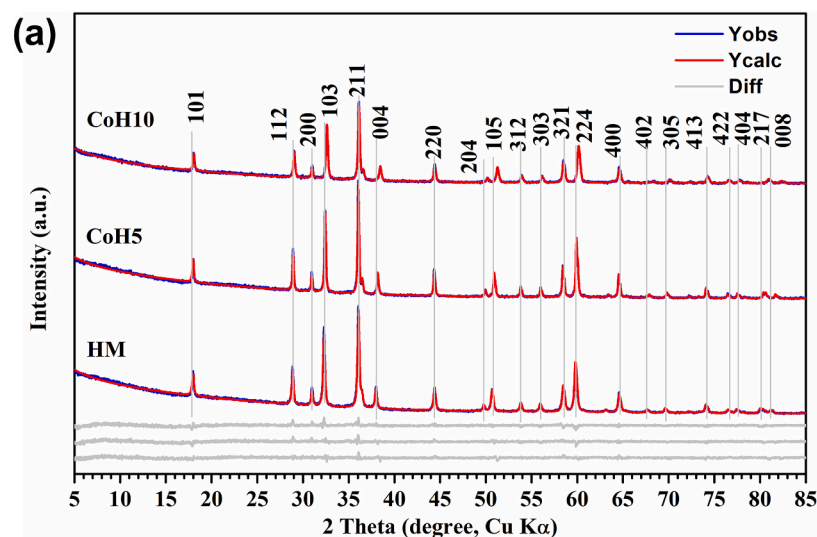
## 2.4. X-ray absorption fine structure (XAFS) spectroscopy

The XAFS data were collected at room temperature on the 1W1B beamline at the Beijing Synchrotron Radiation Facility (BSRF) (Yin et al., 2012). Cobalt K-edge XAFS data were collected in fluorescence mode over the energy range of 7510 to 8305 eV. Reduction and analysis of XAFS data were performed using Athena and Artemis from the IFEFFIT software package (Ravel and Newville, 2006). Cobalt K-edge spectra were background-subtracted using the following parameters:  $E_0 = 7716$  eV,  $R_{bkg} = 1.0$  Å and  $k$ -weight = 2. Structural parameters (bond length (R), coordination number (CN), and Debye-Waller factor ( $\sigma^2$ )) were obtained by fitting the  $k^3$ -weighted EXAFS data to the standard EXAFS equation (Kelly et al., 2008). Phase and amplitude functions were calculated using FEFF7.0 (Rehr et al., 1992). The Co K-edge EXAFS data were fitted in an R space of 1–4 Å over a  $k$  range of 3.1–12.0 Å<sup>-1</sup>, using several single scattering paths calculated by substituting Co for tetrahedral or octahedral Mn in the hausmannite structure (ICSD 76088). An amplitude reduction factor ( $S_0^2$ ) of 0.877 for Co was adopted from our previous studies (Yin et al., 2014). In all fits, the number of independent variables was much smaller than that of the independent data points allowed. During Fourier transformation and EXAFS data fitting, a Hanning window was used.

## 3. Results

### 3.1. Powder XRD

Three synthesized samples display similar XRD patterns (Fig. 1a),



which coincide well with the tetragonal hausmannite standard (ICDD 89-4837). The main characteristic reflections at  $\sim 3.10$  Å,  $\sim 2.77$  Å,  $\sim 2.49$  Å,  $\sim 1.58$  Å, and  $\sim 1.54$  Å can be indexed to (112), (103), (211), (321), and (224), respectively (Giovannelli et al., 2012; Zhao et al., 2011). With an increase in Co content, the peak positions of the ( $hk0$ ) reflections do not change but those of ( $hkl$ ) reflections shift to higher angles, indicating a decrease of unit-cell parameter  $c$ . Rietveld refinements of these samples were performed using the hausmannite structure (ICSD 76088) as the starting model. Because of the similarity of the Co and Mn X-ray scattering factors, the refinements were not able to provide information about ordering of the Co cations over the tetrahedral and octahedral sites or the Co valence. The refinements were thus carried out assuming all Mn, and the results are listed in Fig. 1a and Table S1. From HM to CoH10, unit-cell parameter  $a$  is essentially constant at  $5.771$ – $5.774$  Å, while parameter  $c$  systematically decreases from  $9.477 \pm 0.002$  Å to  $9.370 \pm 0.002$  Å. The indicator of Jahn-Teller distortion of the  $[\text{Mn(III)}\text{O}_6]$  octahedron in hausmannite,  $c/(1.414a)$ , likewise decreases from  $1.1613 \pm 0.0003$  for HM to  $1.1479 \pm 0.0004$  for CoH10, indicating the reduction of Jahn-Teller distortion after Co doping (Bordeneuve et al., 2010; Hirai et al., 2016; Kim et al., 2012). In hausmannite, the  $[\text{Mn(III)}\text{O}_6]$  octahedra are elongated along the  $[001]$  direction (Jarosch, 1987), therefore the decrease in  $c$  and the Jahn-Teller distortion indicator clearly confirm the replacement of lattice  $\text{Mn}^{3+}$  by the smaller  $\text{Co}^{2+/3+}$  and/or  $\text{Mn}^{4+}$  (Bordeneuve et al., 2010; Hirai et al., 2016; Shannon, 1976; Song et al., 2020). The coherent scattering domain (CSD) sizes determined by the refinements for HM, CoH5 and CoH10 are  $59.1 \pm 0.7$  nm,  $91.6 \pm 1.1$  nm and  $74.9 \pm 1.3$  nm, respectively. This may suggest that Co doping promotes the

**Fig. 1.** (a) Powder XRD patterns of HM and Co-doped hausmannite samples, overlaid with the best Rietveld structure refinement results based on a hausmannite model (ICSD 76088). (b) Powder XRD patterns of three years aged Co-doped samples, agedHM and agedCoH10, overlaid with the best calculated patterns by quantitative phase analysis using a hausmannite model (ICDD 76088) and manganite model (ICSD 84949). Blue lines are experimental data ( $Y_{\text{obs}}$ ), red lines are calculated patterns ( $Y_{\text{calc}}$ ), and the light gray lines are the difference patterns (Diff). The reflections of hausmannite are not labeled while the main peak for manganite ( $\gamma$ - $\text{MnOOH}$ ) is indicated by dash line. (c) Crystal diagram of hausmannite (ICSD 76088). (For interpretation of the references to colour in this figure legend, the reader is referred to the web version of this article.)

hausmannite crystal growth at the experimental conditions.

The powder XRD analysis of three years aged HM (agedHM) and CoH10 (agedCoH10) is plotted in Fig. 1b. In addition to the main reflections of hausmannite (ICSD 76088), there is an additional peak at 2 $\theta$  of 26.18 $^\circ$  in agedHM. This peak coincides well with that of manganite (ICSD 84949). This peak also appears in agedCoH10, but with much lower intensity than that in agedHM. This suggests that Co-doped hausmannite sample undergoes slower oxidation at room temperature during aging in the dry state than that of pure hausmannite. Quantitative phase analysis of these aged samples were performed using the hausmannite (ICSD 76088) and manganite structure (ICSD 84949). The results are depicted in Fig. 1b and Table S2. For agedHM, the contents of hausmannite and manganite are 85.9  $\pm$  1.9%, and 14.1  $\pm$  1.9%, respectively. For agedCoH10, the contents of hausmannite and manganite are 97.4  $\pm$  0.7% and 2.6  $\pm$  0.7%, respectively.

### 3.2. Elemental analysis, specific surface areas and morphologies

With increasing Co content, the Mn content decreases from 70.92  $\pm$  0.01% for HM to 69.63  $\pm$  0.32% and 65.93  $\pm$  1.16% for CoH5 and CoH10, respectively. The final Co/Mn molar ratios in these samples are

approximately the same as those in the initial reactants. The specific surface area (SSA) of HM is 12.4 m $^2$ ·g $^{-1}$ , and decreases to 11.7 m $^2$ ·g $^{-1}$  and 11.8 m $^2$ ·g $^{-1}$  for CoH5 and CoH10, respectively.

Fresh HM crystals are composed of irregular cubic particles (Fig. 2a), which is consistent with previous studies (Giovannelli et al., 2012; Hao et al., 2011; Zhang et al., 2011). Co-doped hausmannite crystals are uniformly composed of cubic particles (Fig. 2b, c), which are also similar to Co-doped hausmannite samples in previous studies (Dong et al., 2013). Statistical analysis of the particle sizes of these samples gives an average size of 85  $\pm$  18 nm of HM, 131  $\pm$  27 nm of CoH5 and 103  $\pm$  28 nm of CoH10 (Fig. S1). These physical sizes coincide well with the CSD sizes obtained by powder XRD analysis. Both suggest that Co-doped samples have larger sizes than the pure one. This may indicate that Co ions play a significant role in the growth and assembly of hausmannite initial crystals, and a low amount of Co may favor the crystal growth of hausmannite; but further increasing the Co content will cause structural defects in the mineral structure and thus retard the crystal growth.

In order to confirm whether these Co-doped hausmannite samples are stable during dry storage at room temperature, the HRTEM and SAED patterns of the samples obtained after aging for 3 years, agedHM and agedCoH10, are also presented in Fig. 2d-i. There are plenty of lath-

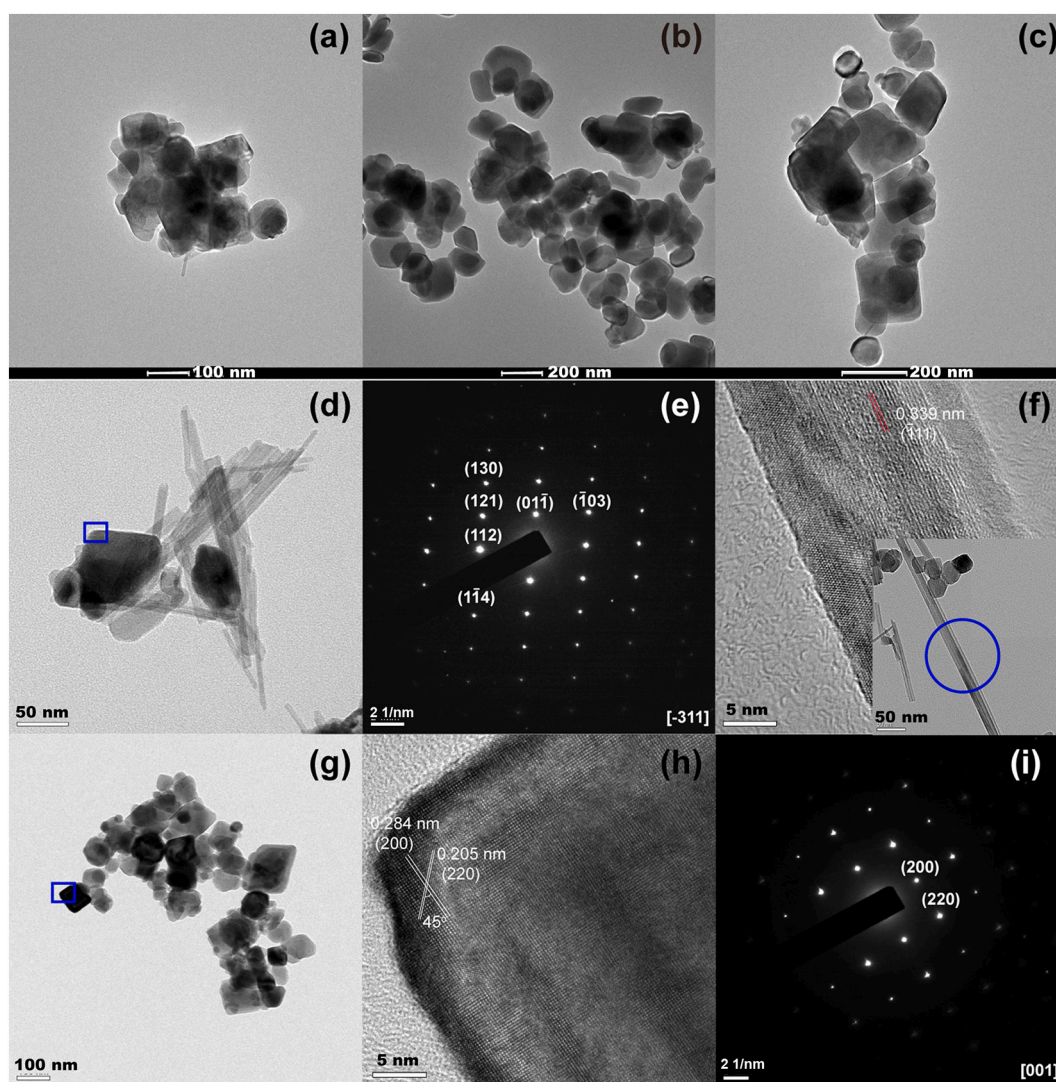


**Fig. 2.** Typical TEM images of freshly prepared Co-doped hausmannite samples (a, HM; b, CoH5; c, CoH10), and 3 years aged samples of (d) agedHM and (g) agedCoH10. (e) and (i) show the SAED patterns of the areas in the blue rectangles in (d) and (g), respectively, while (f) and (h) are typical HRTEM images for the area in the blue circle in the inset at right down of panel (f) and the blue rectangle in panel (g) correspondingly. (For interpretation of the references to colour in this figure legend, the reader is referred to the web version of this article.)

like crystals in agedHM, besides the cubic crystals (Fig. 2d). The SAED pattern of the cubic crystal (Fig. 2e) confirms that the cubes are pure hausmannite single crystals. In the HRTEM image of the lath crystal (Fig. 2f), a lattice distance of 0.339 nm is observed, matching well with that of manganite. The crystals of agedCoH10 retain their cubic shapes for hausmannite (Fig. 2g), which is also confirmed by HRTEM and SAED (Fig. 2h, i).

### 3.3. FTIR

The FTIR spectra of these freshly prepared Co-doped hausmannite samples have four peaks located at 408, 525, 629, and 3415  $\text{cm}^{-1}$  (Fig. 3). These bands coincide well with those of hausmannite (Kirillov et al., 2009). The 3415  $\text{cm}^{-1}$  band is assigned to OH vibrations of physisorbed water molecules, while the three other peaks from left to right correspond to wagging, bending and stretching vibrations of  $[\text{MnO}_6]$  and  $[\text{MnO}_4]$  units (Julien et al., 2004; Kirillov et al., 2009).

After three years aging in the dry state, the spectra of these hausmannites change. Firstly, a peak at 1630  $\text{cm}^{-1}$  appears (Fig. 3). As this peak corresponds to molecular  $\text{H}_2\text{O}$  bending vibrations (Kim et al., 2002), the presence of this peak suggests there is a quantity of physisorbed water on the mineral surfaces and/or in the structures. Secondly, although the main peaks for hausmannite are preserved in the spectrum of agedHM, the relative intensities of the peaks belonging to manganite, such as 440, 484, 597, 1085, 1116, 1152, 2075 and 2655  $\text{cm}^{-1}$  have increased. This indicates a significant portion of hausmannite is transformed into manganite during the aging (Kirillov et al., 2009; Kohler et al., 1997). Additionally, careful inspection of the spectrum of aged-CoH10 shows that, the original 525  $\text{cm}^{-1}$  peak of fresh CoH10 is shifted to 508  $\text{cm}^{-1}$  for agedCoH10, and there are three small additional peaks at 1085, 1116 and 1152  $\text{cm}^{-1}$ , indicating the presence of a minor amount of manganite (Fig. 3e-h). This agrees well with the XRD analysis. Additionally, the bands for agedHM and agedCoH10 are weaker and broader relative to the initial samples, owing to the coexistence of several Mn oxide phases.

### 3.4. Mn 2p XPS spectra

Manganese 2p spectra of these samples are used to investigate the proportions of various Mn species on the mineral surfaces. With Co content increasing, the peak binding energy (BE) shifts to low BE side (Fig. 4a). For example, the Mn 2p<sub>3/2</sub> BE is decreased from 641.94 eV for HM to 641.01 eV for CoH10, indicating the decrease of the Mn average oxidation state (AOS). Further quantitative fitting analysis of the

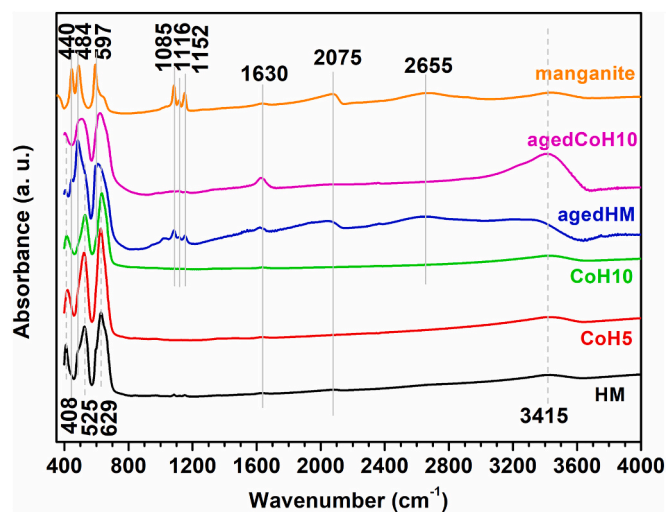


Fig. 3. FTIR spectra of freshly prepared and 3 years aged Co-doped hausmannite samples and a synthesized manganite standard.

spectrum using multiplet parameters (Ilton et al., 2016) are conducted (Fig. 4b, c and Table S3). The HM spectrum can be decomposed to 28%  $\text{Mn}^{2+}$ , 58%  $\text{Mn}^{3+}$  and 14%  $\text{Mn}^{4+}$ . With the increase of the dopant level, the relative proportions of  $\text{Mn}^{3+}$  and  $\text{Mn}^{4+}$  are decreased but that of  $\text{Mn}^{2+}$  is increased. The spectrum of CoH10 can be decomposed to 39%  $\text{Mn}^{2+}$ , 54%  $\text{Mn}^{3+}$  and 7%  $\text{Mn}^{4+}$ . The calculated Mn AOSs are  $2.86 \pm 0.02$  and  $2.69 \pm 0.02$  for HM and CoH10, respectively.

### 3.5. Acid dissolution experiments

Fig. 5 shows the fraction of dissolved Co or Mn ( $\chi_{\text{Co}}$  or  $\chi_{\text{Mn}}$ ) vs. time, and  $\chi_{\text{Co}} - \chi_{\text{Mn}}$  curves of the Co-doped samples in 2 M HCl solution at room temperature. For both samples, the  $\chi_{\text{Co}}$  or  $\chi_{\text{Mn}}$  vs. time curves show a fast initial rate, followed by a gradual decrease until the dissolution is complete, and the dissolution of Co is slightly quicker than that of Mn. To obtain the Mn and Co dissolution rate constant (K), Kabai equation,  $\chi_{\text{Metal}} = 1 - \exp(-K \cdot t^{\alpha})$ , is employed to model the dissolution curves (Alvarez et al., 2007; Liu et al., 2019). With Co content increasing, the Mn dissolution rate constant ( $K_{\text{Mn}}$ ) is decreased from  $0.2823 \pm 0.0301 \text{ min}^{-1}$  for CoH5 to  $0.2070 \pm 0.0175 \text{ min}^{-1}$  for CoH10. These results indicate that doping Co makes the mineral structure more stable and more resistant to proton attack. This may be related to the higher bond dissociation energy (BDE) of Co-O ( $397 \pm 9 \text{ kJ} \cdot \text{mol}^{-1}$ ) than that of Mn-O ( $362 \pm 25 \text{ kJ} \cdot \text{mol}^{-1}$ ) (Lide and Haynes, 2010). According to the BDE, it is expected that Mn cations will be slightly easier to be released out of the lattice than Co cations. In contrast, the dissolution-rate constant of Co is much higher than that of Mn, and increases with increasing the Co content in the sample. The Co dissolution rates ( $K_{\text{Co}}$ ) in these samples are  $0.6516 \pm 0.0724 \text{ min}^{-1}$  for CoH5 and  $0.8743 \pm 0.0804 \text{ min}^{-1}$  for CoH10, respectively. This may suggest that Co may not occupy completely the same lattice sites as Mn. But it should also be noteworthy that, the mineral dissolution in HCl solution is a much complex process, which involves protonation, complexation, and reduction induced dissolutions by  $\text{Cl}^-$  (Cornell and Schwertmann, 2003). It can be affected by many other factors such as crystal sizes, coexisted cations,  $\text{H}^+$  concentration and so on. Particles with smaller crystal sizes are dissolved faster than those with large crystal sizes (Alvarez et al., 2007; Cornell and Schwertmann, 2003). The obtained  $\alpha$  values for  $\chi_{\text{Co-t}}$  or  $\chi_{\text{Mn-t}}$  for CoH5 and CoH10 are also the same, confirming the purity of these minerals. Further, the  $\chi_{\text{Co}} - \chi_{\text{Mn}}$  curves are a little convex with respect to the  $Y = X$  line. This suggests Co incorporates into the mineral structures but is slightly preferentially enriched in the rims of the crystals (Qin et al., 2017; Yin et al., 2014).

### 3.6. Co K-edge XAFS analysis

#### 3.6.1. X-ray adsorption near edge structure (XANES)

The Co K-edge XANES profiles of the two Co-doped hausmannite samples, CoH5 and CoH10, are distinct from but intermediate between those of the reference compounds  $\text{CoSO}_4$  and  $\text{CoOOH}$  (Fig. 4d), suggesting a mixed-valence of Co in these samples. Linear combination fitting analysis further quantitatively confirms this (Fig. 4d and Table S4). The results show that CoH5 and CoH10 both contain 66–67%  $\text{Co}^{3+}$  and 33–34%  $\text{Co}^{2+}$ . Previous studies reported that Co exists as only  $\text{Co}^{2+}$  in Co-containing hausmannite ( $\text{Mn}_{3-x}\text{Co}_x\text{O}_4$ ,  $0 < x < 1$ ) samples synthesized under mild alkaline conditions and at high temperature (Bordeneuve et al., 2010; Dong et al., 2013; Hirai et al., 2016). In contrast, the samples used here were synthesized using a coprecipitation method at room temperature and at  $\text{pH} > 10$ .

#### 3.6.2. EXAFS

The  $k^3$ -weighted Co K-edge EXAFS and the corresponding Fourier transformed spectrum (FT) of typical Co-doped sample, CoH10, are different from those of  $\text{CoOOH}$  and  $\text{CoSO}_4$  references (Yin et al., 2015), indicating neither  $\text{CoOOH}$  precipitate nor free  $\text{Co}^{2+}$  exists (Fig. 6a,b). As both powder XRD analysis and acid dissolution confirm the

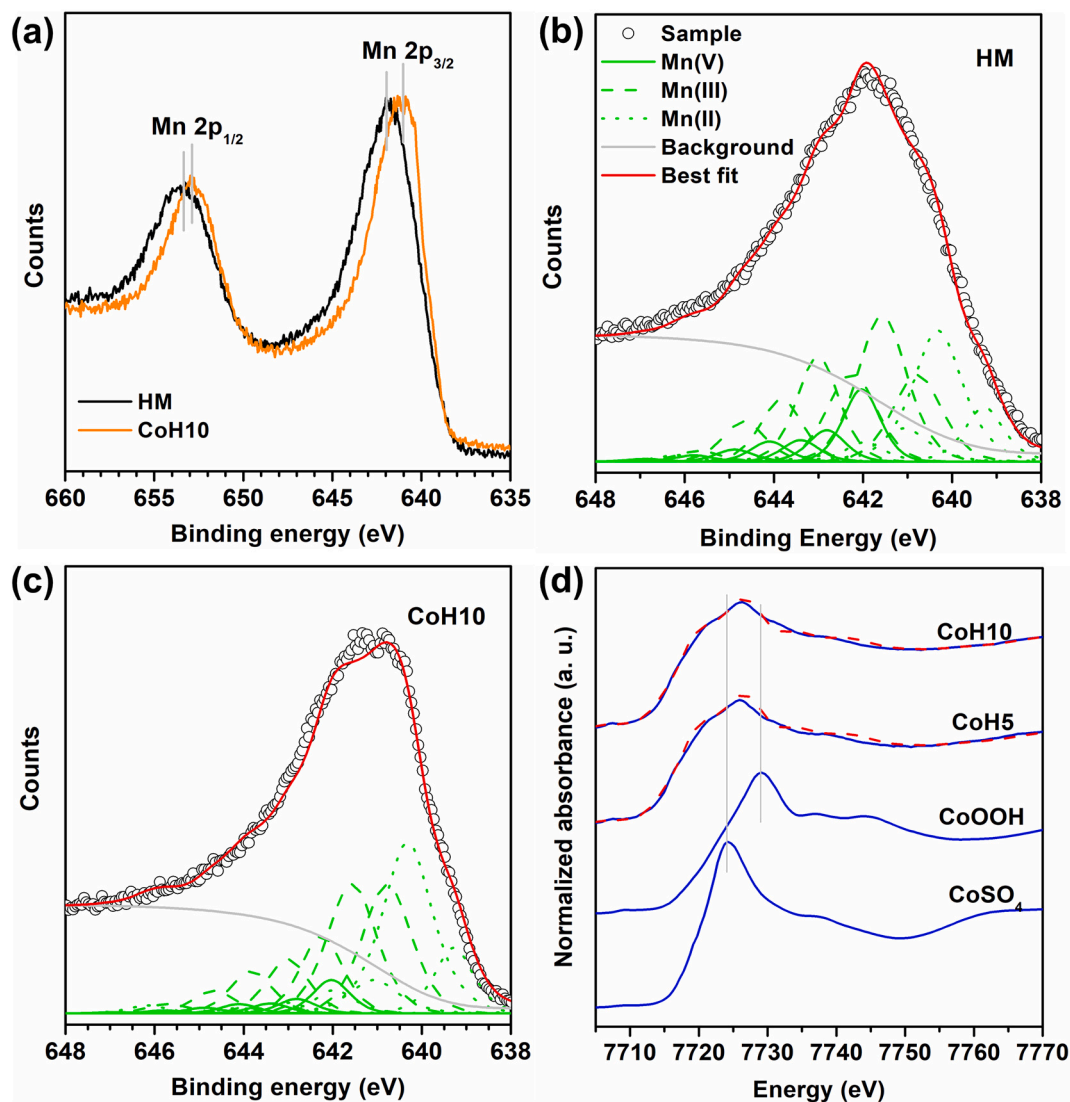


Fig. 4. Mn 2p spectra of HM and CoH10 (a), and the corresponding Mn 2p<sub>3/2</sub> spectra (b, c) with the best fit overlaid (The black open circles represent experimental data, red lines are the best fit to the data, peaks corresponding to Mn<sup>2+</sup>, Mn<sup>3+</sup> and Mn<sup>4+</sup> are shown as green dot, dash and solid lines respectively, and the gray solid lines at the bottom are the difference patterns). (d) Linear combination fitting (red dashed lines) of Co K-edge XANES spectra of CoH5 and CoH10, using CoSO<sub>4</sub> and CoOOH (Yin et al., 2015 #50) as references. (For interpretation of the references to colour in this figure legend, the reader is referred to the web version of this article.)

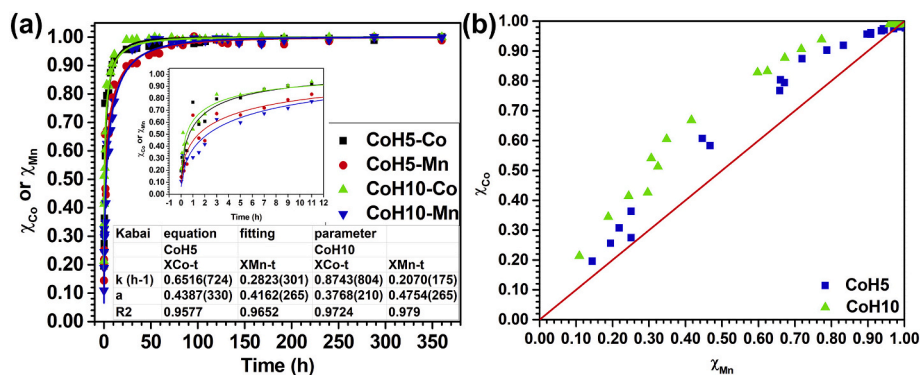
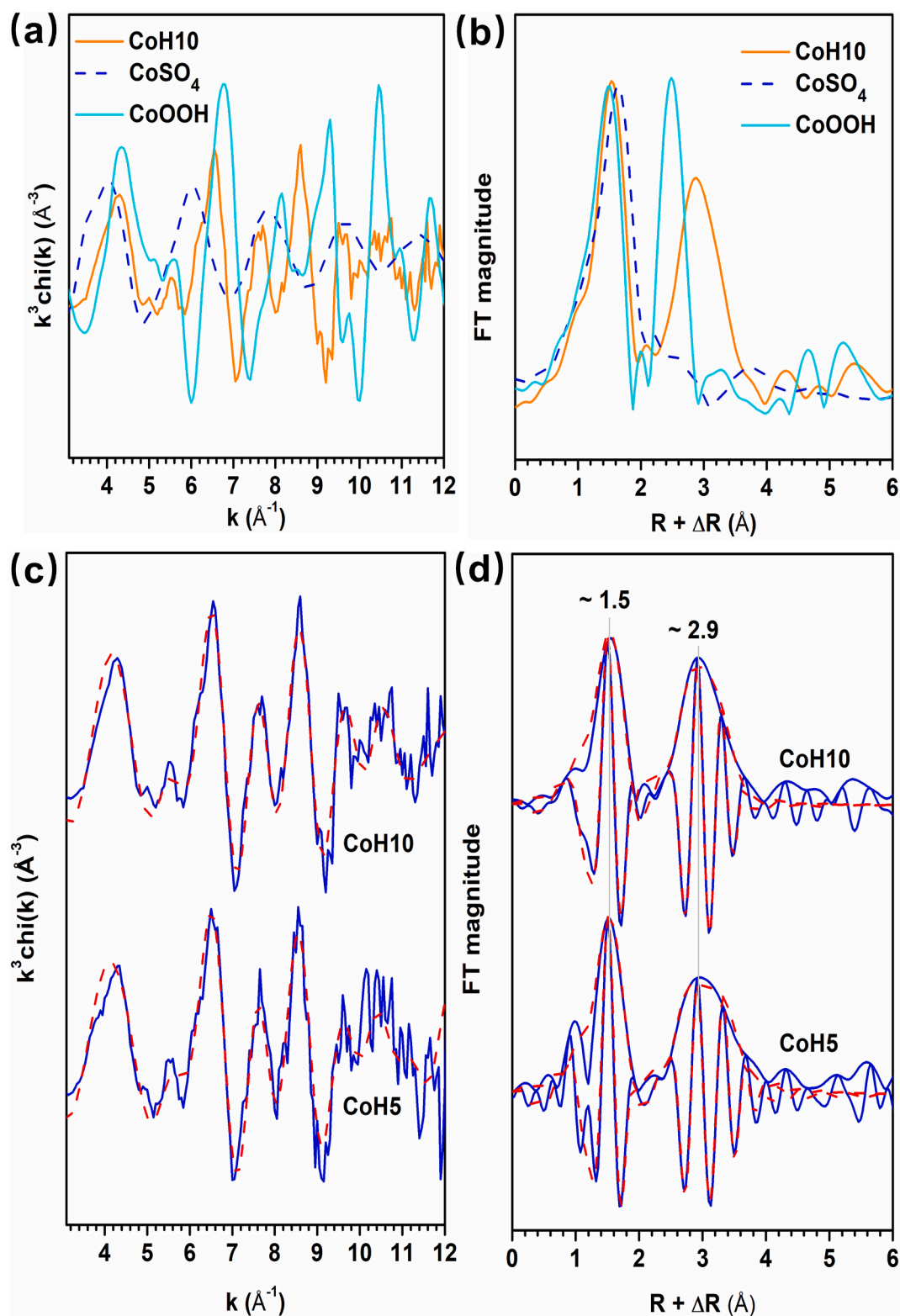


Fig. 5. (a) Mineral dissolution kinetic curves expressed as %Co dissolved ( $\chi_{Co}$ ) or %Mn dissolved ( $\chi_{Mn}$ ) in 2 M HCl solution at 25 °C and (b) the corresponding  $\chi_{Co}$  versus  $\chi_{Mn}$  curves of these Co-doped hausmannite samples. In panel a, the inset is the detailed figure in the first 12 h of the dissolution reactions, the solid lines are the best fit of the whole dissolution curve with Kabai equation,  $\chi_{Co(Mn)} = 1 - \exp.(-kt)^\alpha$ , in which k and  $\alpha$  are constants representing the dissolution rate constant and the characteristics of the mineral structure, and the corresponding fitting parameters are listed in the table inserted in the panel. In panel b, the red solid line is the 1:1 line. (For interpretation of the references to colour in this figure legend, the reader is referred to the web version of this article.)

incorporation of Co into the mineral structures, Co can exist in either an octahedral or a tetrahedral coordination or both. The oscillations of CoH5 and CoH10 are essentially the same (Fig. 6c,d), indicating that Co

ions in the two samples have similar coordination environments. The corresponding FTs show two strong backscattering neighbors at  $R + \Delta R \sim 1.5 \text{ \AA}$  and  $\sim 2.9 \text{ \AA}$ . The former corresponds to the first Co-O pair, and



**Fig. 6.** Comparison of  $k^3$ -weighted Co K-edge EXAFS (a) and the corresponding Fourier transformed (FTs) spectra (b) of CoH10 and that of synthesized  $\text{CoSO}_4$  and  $\text{CoOOH}$  from our previous study (Yin et al., 2015). In panel b, the magnitudes of first Co-O peaks were normalized. The Co K-edge EXAFS (c) and the corresponding Fourier transformed (FTs) spectra (d) of CoH5 and CoH10, overlaid with the best fitting by assuming that all the Co cations occupy the octahedral sites. Blue lines are experimental data and dashed red lines are the best fits. (For interpretation of the references to colour in this figure legend, the reader is referred to the web version of this article.)

the later can be deconvoluted into several Co-Me (Me = Mn and Co) pairs (Bordeneuve et al., 2010).

To obtain more detailed information about the local structures of Co in the Co-doped hausmannite samples, the Co K-edge EXAFS spectra of CoH5 and CoH10 are analyzed with shell-by-shell fits (Fig. 6c, d and Table 1). The results indicate an average Co-O distance of  $1.97 \pm 0.02 \text{ \AA}$ , which is slightly longer than those ( $1.90\text{--}1.91 \text{ \AA}$ ) previously reported for octahedral  $\text{Co}^{3+}$  (Manceau et al., 1997; Yin et al., 2013; Yin et al., 2015), but much shorter than for octahedral  $\text{Co}^{2+}$  ( $2.09 \text{ \AA}$ ) (Manceau et al., 1997). This further suggests the coexistence of  $\text{Co}^{3+}$  and  $\text{Co}^{2+}$  in the hausmannites. Although cations in tetrahedral coordination, such as  $\text{Zn}^{2+}$ , typically form shorter distances with the first coordination O (Kwon et al., 2009), the case for Co is complex. It was reported that in  $\text{YBaCo}_4\text{O}_7$ , the average tetrahedral Co-O distance ranges from  $1.90\text{--}1.92 \text{ \AA}$  (Valldor and Andersson, 2002). Thus, it is difficult to distinguish octahedral from tetrahedral Co based on Co-O distances alone. The fits also indicate longer Co-Me (Me = Co, Mn) correlations at radial distances of  $2.80\text{--}2.82$ ,  $3.01\text{--}3.02$ ,  $3.36\text{--}3.38$  and  $3.77\text{--}3.78 \text{ \AA}$  (Table 1). These values correspond to the distances between edge-sharing octahedra in the *a*- and *c*-direction, and corner-sharing octahedron-tetrahedron pairs in the *a*- and *c*-direction, respectively, matching well with those for Co located in the octahedron sites (Table S1). Further, when comparing to the corresponding average Me-Me distances obtained by Rietveld structure refinements (Table S1), these Co-Me distances are shorter, owing to the smaller radius of Co(III) (Shannon, 1976).

EXAFS fittings assuming that all the Co cations occupy the tetrahedral sites are also conducted. An average Co-O distance of  $1.96 \pm 0.01 \text{ \AA}$  is derived, which is almost the same as that determined assuming all octahedral Co. An attempt to fit the  $R + \Delta R \sim 2.9 \text{ \AA}$  peak by combining four paths: two paths for octahedron-tetrahedron corner-sharing pairs in the *a*- and *c*-axis, a path for the nearest tetrahedron-tetrahedron pairs and a Co-O path corresponding to that between the center Mn in a tetrahedron and its second shell O belonging to the corner-sharing octahedron, does not yield a reasonable fit. This suggests that the vast majority of Co cations occupy the octahedral sites in Co-doped

**Table 1**  
Co K-edge EXAFS structural parameters obtained from the fit of Co-doped hausmannites.

Octahedron	CoH5	CoH10
Co-O		
CN <sup>a</sup>	6	6
R ( $\text{\AA}$ ) <sup>a</sup>	1.968	1.970(12)
$\sigma^2$ ( $\text{\AA}^2$ ) <sup>a</sup>	0.0067(12)	0.0072
Co-Mn(Co) <sub>OESx</sub> <sup>b</sup>		
CN	2	2
R ( $\text{\AA}$ )	2.821(65)	2.798(43)
$\sigma^2$ ( $\text{\AA}^2$ )	0.0110(63)	0.0113(35)
Co-Mn(Co) <sub>OESz</sub> <sup>b</sup>		
CN	4	4
R ( $\text{\AA}$ )	3.023(44)	3.005(29)
$\sigma^2$ ( $\text{\AA}^2$ )	0.0110(63)	0.0113(35)
Co-Mn(Co) <sub>OTCSx</sub> <sup>b</sup>		
CN	4	4
R ( $\text{\AA}$ )	3.360	3.383(19)
$\sigma^2$ ( $\text{\AA}^2$ )	0.0068(30)	0.0055(11)
Co-Mn(Co) <sub>OTCSz/TT</sub> <sup>b</sup>		
CN	2	2
R ( $\text{\AA}$ )	3.779(24)	3.771(19)
$\sigma^2$ ( $\text{\AA}^2$ )	0.0011(17)	0.0032(17)
E <sub>0</sub> (eV)	-3.4(33)	-1.9(21)
Chi Sq.	126.39	91.27
R factor	0.0617	0.0233

<sup>a</sup> CN = coordination number; R = interatomic distance;  $\sigma^2$  = Debye-Waller factor; E<sub>0</sub> = energy shift; Chi Sq. = chi-squared statistic.

<sup>b</sup> OES<sub>x</sub> and OES<sub>z</sub> refer to edge-sharing octahedra in the *x*- and *z*-axis; OTCS<sub>x</sub> and OTCS<sub>z</sub> refer to octahedron-tetrahedron corner-sharing pairs in the *x*- and *z*-axis; TT refers to the nearest tetrahedron-tetrahedron pairs.

hausmannites (Song et al., 2020).

## 4. Discussion

### 4.1. Co valence and crystal chemistry in Co-doped hausmannite

Cobalt K-edge XANES analysis showed that  $\text{Co}^{2+}$  and  $\text{Co}^{3+}$  coexist in the Co-doped hausmannites. Interestingly, the  $\text{Co}^{3+}/\text{Co}^{2+}$  ratios keep almost the same,  $\sim 2$ , for CoH5 and CoH10. Owing to the high redox potential of  $\text{Co}^{3+}/\text{Co}^{2+}$  pair ( $E^0 = 1.92 \text{ V}$ ) (Lide and Haynes, 2010), O<sub>2</sub> and high valence Mn in the mineral, and surface catalytic oxidation may account for the  $\text{Co}^{2+}$  oxidation. The oxidation of  $\text{Co}^{2+}$  is highly related to the solution conditions, e.g. pH and temperature. Generally, a high concentration of OH<sup>-</sup> and high temperature favors the oxidation (Alvarez et al., 2008; Pozas et al., 2004; Yin et al., 2020b). The coexistence of  $\text{Co}^{2+}$  and  $\text{Co}^{3+}$  in the doped hausmannite samples is similar to that observed in Co-doped goethite samples in our previous study (Yin et al., 2020a), both owing to the low alkalinity and low temperature used. However, in the Co-doped goethite series, the  $\text{Co}^{3+}/\text{Co}^{2+}$  ratio increases with increasing initial Co concentration. This is ascribed to the catalytic oxidation of  $\text{Co}^{2+}$  on the mineral precursor (e.g. ferrihydrite) surfaces driven by the electric potential energy, which is dependent on the redox cation concentration (Boland et al., 2013; Lan et al., 2017; Yin et al., 2020a). The constant  $\text{Co}^{3+}/\text{Co}^{2+}$  ratio here may possibly be explained by the absence of surface catalytic oxidation behaviors on hausmannite surfaces, because hausmannite is an insulator (Bordeneuve et al., 2010).

Powder XRD, acid dissolution experiments and Co K-edge EXAFS analysis demonstrate that the Co cations are incorporated into the mineral structures. In hausmannite,  $\text{Mn}^{2+}$  occupies the tetrahedral site while  $\text{Mn}^{3+}$  occupies the octahedral sites. However, when exotic cations are incorporated into the structure, the crystal chemistry of the exotic cations are complex. Structure analysis of cobalt manganese oxide spinel ( $\text{Mn}_{3-x}\text{Co}_x\text{O}_4$ ) ( $0 \leq x \leq 3$ ) synthesized at  $800 \text{ }^\circ\text{C}$  demonstrates that the tetrahedral Mn is first preferentially substituted by Co for  $x < 1$ , and then the octahedral Mn is replaced by Co with increasing *x* value. It also shows that  $\text{Mn}^{2+}$  and/or  $\text{Co}^{2+}$  fill the tetrahedral sites while  $\text{Mn}^{3+}$ ,  $\text{Co}^{2+}$ , low-spin state  $\text{Co}^{3+}$  and  $\text{Mn}^{4+}$  occupy the octahedral site (Bordeneuve et al., 2010). For a series of  $\text{Mn}_{3-x}\text{Co}_x\text{O}_4$  samples ( $0 \leq x \leq 1.5$ ) synthesized at  $\sim 20 \text{ }^\circ\text{C}$  by coprecipitation of the mixtures of  $\text{Mn}^{2+}$  and  $\text{Co}^{2+}$  solution using  $\text{NH}_3\cdot\text{H}_2\text{O}$ , the Mn(III)O<sub>6</sub> distortion indicator,  $c/\sqrt{2a}$ , almost overlaps with those for the samples from the previous study when  $x < 1$ , and Co cations in these samples was thought to solely occupy the tetrahedral sites (Hirai et al., 2016). Comparison of the  $c/\sqrt{2a}$  of the Co-doped hausmannite samples in the present study with those from previous studies indicates that there is a good linear relationship between Co content and  $c/\sqrt{2a}$  for all these samples when  $x < 1$ , but the dependence of  $c/\sqrt{2a}$  to the sample Co content varies much. The  $c/\sqrt{2a}$  of our samples decreases much faster with increasing Co content than that in literatures, with a slope  $\sim 2$  times that of the later (Fig. 7). This may indicate that the crystal chemistry of Co in our samples is not the same as that in the previous studies, owing to the fact that the mineral preparation method will affect the detailed crystal chemistry of Co (Zhao et al., 2017).

Further, there is a debate in the spin state of the cations in the hausmannite structure. Some literatures reported that in the distorted spinel structure of hausmannite,  $\text{Mn}^{2+}$  is in the low-spin state (LS) while  $\text{Mn}^{3+}$  is in the high-spin state (HS) (Bordeneuve et al., 2010; Jarosch, 1987; Nogués and Poix, 1974). However, other studies adopted that  $\text{Mn}^{3+}$  in hausmannite octahedral sites has a low-spin state while  $\text{Mn}^{2+}$  in tetrahedral sites has a high-spin state (Boucher et al., 1971; Xu et al., 2005). According to molecular orbital calculations, if the  $\text{MnO}_6^{9-}$  cluster has smaller exchange splitting of the  $2t_{2g}$  orbital and larger crystal field splitting, a transition of Mn(III) from HS to LS can occur, in company with a decrease of Mn-O distance from  $2.04$  to  $1.88 \text{ \AA}$  (Sherman, 1984). The average Mn-O distances in  $[\text{Mn(III)O}_6]$  in our Co-doped



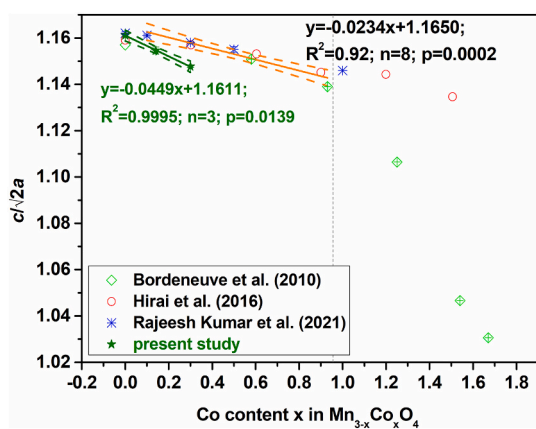


Fig. 7. Comparison of the  $c/\sqrt{2a}$  of the Co-doped hausmannite samples in the present study with those of the  $\text{Mn}_{3-x}\text{Co}_x\text{O}_4$  nanoparticles from previous studies (Bordeneuve et al., 2010; Hirai et al., 2016; Rajeesh Kumar et al., 2021). The solid lines represent the linear fitting of these data with  $x < 1$ .

hausmannites are 2.05–2.06 Å (Table S1). This probably suggests that Mn(III) in our hausmannites are probably HS. In the normal spinel structure of  $\text{Co}_3\text{O}_4$ , HS  $\text{Co}^{2+}$  occupies the tetrahedral sites while LS  $\text{Co}^{3+}$  occupies the octahedral sites (Spencer and Schroeder, 1974). In order to elucidate the possible distributions of various cations in these Co-doped hausmannite samples, the basic physicochemical properties of these cations are compared (Table 2).

After Co doping, the proportions of  $\text{Mn}^{3+}$  and  $\text{Mn}^{4+}$  are decreased while that of  $\text{Mn}^{2+}$  is increased with increasing dopant content. It is generally assumed that  $\text{Co}^{3+}$  in octahedral sites exists mostly in the LS state (Burns, 1993; McKenzie, 1970; Yin et al., 2013). The CFSE of LS  $\text{Co}^{3+}$  (534.2  $\text{kJ}\cdot\text{mol}^{-1}$ ) is  $\sim 2.5$  times larger than that of  $\text{Mn}^{3+}$  in the hausmannite structure, and therefore, it is favorable for  $\text{Co}^{3+}$  to replace  $\text{Mn}^{3+}$ . This is the same for LS  $\text{Co}^{2+}$ . The CFSE of octahedrally coordinated LS  $\text{Co}^{2+}$  (198.2  $\text{kJ}\cdot\text{mol}^{-1}$ ) is larger than that of HS  $\text{Mn}^{3+}$  in hausmannite, favoring the substitution of  $\text{Mn}^{3+}$  by  $\text{Co}^{2+}$ . This is supported by the Co K-edge EXAFS analysis. Further, as the radius of LS  $\text{Co}^{3+}$  in octahedral coordination is 12.7% smaller than that of HS  $\text{Mn}^{3+}$ , this substitution also accounts for the decrease of unit-cell parameter  $c$  and the suppression of the Jahn-Teller distortion. Further, the smaller CFSE of tetrahedral HS Co(II) (58.7  $\text{kJ}\cdot\text{mol}^{-1}$ ) than that of LS Mn(II)

(79.6  $\text{kJ}\cdot\text{mol}^{-1}$ ) in tetrahedron excludes the substitution of Co(II) for tetrahedral Mn(II). Consequently, it is assumed that in the Co-doped hausmannite samples low-spin  $\text{Co}^{2+}$  and  $\text{Co}^{3+}$  occupy the octahedral sites.

#### 4.2. Hausmannite transformation during aging

After aging the pure hausmannite (HM) and Co-doped hausmannite (CoH10) in dry state for three years,  $14.1 \pm 1.9\%$  of manganite appears in agedHM while  $2.6 \pm 0.7\%$  of manganite is observed in agedCoH10. This clearly suggests the transformation of hausmannite to manganite. It is proposed that the transformation of hausmannite to manganite involves  $\text{O}_2$  and  $\text{H}_2\text{O}$  according to the following equation (Eq. (1)):



During hausmannite aging in dry state, Mn(II) on the mineral surfaces are gradually oxidized by  $\text{O}_2$  to form  $-\text{Mn} = \text{O}$  groups. Then these groups react with physisorbed  $\text{H}_2\text{O}$ , leading to the formation of  $-\text{Mn} = (\text{OH})_2$  groups. Finally  $-\text{Mn} = (\text{OH})_2$  groups are transformed to  $\text{MnOOH}$ , which is thought to be the rate-determining step (Kirillov et al., 2009).

This transformation processes can be affected by many factors. In the present study, the  $\text{O}_2$  and  $\text{H}_2\text{O}$  concentrations are limited during hausmannite aging, which is stored in a closed tube. Thus the transformation rate here is much lower than those in air (Kirillov et al., 2009) and in high relative humidity (Rabiei et al., 2005). However, the transformation rate of CoH10 is much lower than that of HM at same conditions. This may be related to the substitution-induced changes in mineral physicochemical properties, such as chemical composition, particle size and stability of the host mineral. Although Co-doped hausmannite samples here show the same cubic morphology as that of pure hausmannite, statistical analyses of TEM determined particle sizes and the CSDs obtained by XRD show that the Co-doped crystals are larger than those of HM. The increase in crystal sizes of CoH5 and CoH10 may make them more stable than HM (Birkner and Navrotsky, 2014; Gillot et al., 2001), since smaller crystallite size is reported to promote phase transformation (Birkner and Navrotsky, 2012; Birkner and Navrotsky, 2014). Additionally, doping Co decreases the  $\text{Mn}^{3+}$  content, and suppresses the Jahn-Teller distortion to make the mineral structure more stable than pure one. The decrease of  $\text{Mn}^{3+}$  may also favor the formation of hausmannite rather than  $\text{MnOOH}$  phase (Jha et al., 2012). Our results clearly show that, exotic cation substitution have great impact on the transformation of hausmannite. Conclusively, the enrichment of various TMs

Table 2

Electron structure, octahedral coordination radius (CR), electronegativity ( $\chi$ ), ionization potential ( $\eta$ ), crystal field stabilization energy (CFSE), pairing energy (P) and bond dissociation energy (BDE) of Mn and Co.

Cation		Electronic structure	Configuration	CR (Å) <sup>a</sup>	$\chi^b$	$\eta^c$ (eV)	$\Delta^d$ (kJ/mol)	CFSE <sup>d</sup> (kJ/mol)	P <sup>e</sup> (kJ/mol)	BDE <sup>e</sup> (kJ/mol)		
Mn	II	3d <sup>5</sup>	4(LS)	(e) <sup>4</sup> (t <sub>2</sub> ) <sup>1</sup>	–	–	33.7	39.8	79.6	285.0	362 ± 25	
			4(HS)	(e) <sup>2</sup> (t <sub>2</sub> ) <sup>3</sup>	0.80	1.4934	–	0				
			6(LS)	(t <sub>2g</sub> ) <sup>5</sup>	0.81	1.4903	89.8	179.6				
	III	3d <sup>4</sup>	6(HS)	(t <sub>2g</sub> ) <sup>3</sup> (e <sub>g</sub> ) <sup>2</sup>	0.97	1.4407	–	0				
			4(LS)	(e) <sup>4</sup>	–	–	51.2	111.6	290.2			301.6
			4(HS)	(e) <sup>2</sup> (t <sub>2</sub> ) <sup>2</sup>	–	–	–	67.0				
Co	II	3d <sup>7</sup>	6(LS)	(t <sub>2g</sub> ) <sup>4</sup>	0.72	1.7052	251.3	402.1				
			6(HS)	(t <sub>2g</sub> ) <sup>3</sup> (e <sub>g</sub> ) <sup>1</sup>	0.785	1.6753	–	150.8				
			4(LS)	(e) <sup>4</sup> (t <sub>2</sub> ) <sup>3</sup>	–	–	33.5	48.9	58.7	250	397 ± 9	
	III	3d <sup>6</sup>	4(HS)	(e) <sup>4</sup> (t <sub>2</sub> ) <sup>3</sup>	0.72	1.5882	–	58.7				
			6(LS)	(t <sub>2g</sub> ) <sup>6</sup> (e <sub>g</sub> ) <sup>1</sup>	0.79	1.5665	110.1	198.2				
			6(HS)	(t <sub>2g</sub> ) <sup>5</sup> (e <sub>g</sub> ) <sup>2</sup>	0.885	1.5371	–	88.1				
III	3d <sup>6</sup>	6(LS)	(t <sub>2g</sub> ) <sup>6</sup>	0.685	1.7913	248.4	534.2	282.6				
		6(HS)	(t <sub>2g</sub> ) <sup>4</sup> (e <sub>g</sub> ) <sup>2</sup>	0.75	1.7614	–	89.0					

<sup>a</sup> Data adopted from Shannon (1976).

<sup>b</sup> Data calculated according to Portier et al. (1994).

<sup>c</sup> Data from Lide and Haynes, 2010.

<sup>d</sup> Data from Burns (1993) and Huheey et al. (1993). These data were calculated by neglecting the electron pairing energies and electron-electron effects for simplification.

<sup>e</sup> Data from Huheey et al. (1993). These values are for the free ions and may be 15–30% smaller when cations are chemically coordinated because of the nephelauxetic effects.

in hausmannite may be an important reason for the stability of these minerals in natural environments.

## 5. Conclusions and environmental implications

Natural hausmannite analogs, including Co-substituted hausmannites with Co/Mn molar ratios of 0.05 and 0.11 were synthesized at ambient conditions. Cobalt ions existed as  $\text{Co}^{3+}$  and  $\text{Co}^{2+}$ , substituting for  $\text{Mn}^{3+}$  in the octahedral sites, which resulted in suppression of the Jahn-Teller distortion and a commensurate decrease in the unit-cell parameter  $c$ . These Co-doped hausmannite samples had decreased Mn AOS and increased crystal sizes than HM. Acid dissolution experiments confirmed that Co incorporated into the mineral structures, and made the mineral more stable. Cobalt K-edge EXAFS analysis demonstrated that dopants occupied the octahedral sites in the hausmannite structure. Cobalt doping greatly improved the hausmannite stability during dry aging at room temperature. After three years of aging in a dry state,  $14.1 \pm 1.9\%$  of hausmannite in HM was transformed to manganite, while only  $2.6 \pm 0.7\%$  of hausmannite in CoH10 was transformed to manganite.

Based on the excellent adsorption, reducing and oxidizing reactivity towards a variety of metal pollutants (Antao et al., 2019; Baron et al., 1998; Bordeneuve et al., 2010; Green et al., 2004; Lefkowitz and Elzinga, 2015; Song et al., 2020), hausmannite may play an important role in mediating the mobility and fate of metal nutrients and contaminants in terrestrial environments. The substitution of TM for lattice Mn in the hausmannite structure may greatly modify the mineral physicochemical properties and thus their reactivity. Carefully and accurately investigation of the reactivity of these doped minerals, which are close to their natural analogues, with nutrients and pollutants, may help us understand and predict the geochemical behaviors of elements of interest in natural settings and also benefit us from the design and application of environmental-friendly Mn oxide materials in pollutant control and remediation.

## Declaration of Competing Interest

The authors declare that they have no known competing financial interests or personal relationships that could have appeared to influence the work reported in this paper.

## Acknowledgments

We gratefully acknowledge Dr. Wei Zhao from Northwest A&F University for providing the FTIR data of manganite. The authors gratefully thank the Key science and technology projects of Inner Mongolia autonomous region (2019ZD001), the National Natural Science Foundations of China (Nos.42077015 and 41771267), the National Key Research and Development Program of China (No. 2016YFD0800403), and the Fundamental Research Funds for the Central Universities (Grant 103-510320036) for the financial support.

## Appendix A. Supplementary data

Supplementary data to this article can be found online at <https://doi.org/10.1016/j.chemgeo.2021.120448>.

## References

- Alvarez, M., Rueda, E.H., Sileo, E.E., 2007. Simultaneous incorporation of Mn and Al in the goethite structure. *Geochim. Cosmochim. Acta* 71 (4), 1009–1020.
- Alvarez, M., Sileo, E.E., Rueda, E.H., 2008. Structure and reactivity of synthetic Co-substituted goethites. *Am. Mineral.* 93 (4), 584–590.
- Antao, S.M., Cruickshank, L.A., Hazrah, K.S., 2019. Structural trends and solid-solutions based on the crystal chemistry of two hausmannite ( $\text{Mn}_3\text{O}_4$ ) samples from the Kalahari manganese field. *Minerals* 9 (6), 343.
- Baron, V., Gutzmer, J., Rundlof, H., Tellgren, R., 1998. The influence of iron substitution on the magnetic properties of hausmannite,  $\text{Mn}^{2+}(\text{Fe,Mn})_2(\text{OH})_4$ . *Am. Mineral.* 83 (7–8), 786–793.
- Barreto, M.S.C., Elzinga, E.J., Alleoni, L.R.F., 2020. Hausmannite as potential As(V) filter. Macroscopic and spectroscopic study of As(V) adsorption and desorption by citric acid. *Environ. Pollut.* 262, 114196.
- Birkner, N., Navrotsky, A., 2012. Thermodynamics of manganese oxides: Effects of particle size and hydration on oxidation-reduction equilibria among hausmannite, bixbyite, and pyrolusite. *Am. Mineral.* 97 (8–9), 1291–1298.
- Birkner, N., Navrotsky, A., 2014. Rapidly reversible redox transformation in nanophase manganese oxides at room temperature triggered by changes in hydration. *Proc. Natl. Acad. Sci.* 111 (17), 6209–6214.
- Boland, D.D., Collins, R.N., Glover, C.J., David Waite, T., 2013. An in situ quick-EXAFS and redox potential study of the Fe(II)-catalysed transformation of ferrihydrite. *Colloids Surf. A Physicochem. Eng. Asp.* 435, 2–8.
- Bordeneuve, H., Tenailleau, C., Guillemet-Fritsch, S., Suard, E., Rousset, A., 2010. Structural variations and cation distributions in  $\text{Mn}_{3-x}\text{Co}_x\text{O}_4$  ( $0 \leq x \leq 3$ ) dense ceramics using neutron diffraction data. *Solid State Sci.* 12 (3), 379–386.
- Boucher, R., Buhl, R., Perrin, M., 1971. Propriétés et structure magnétique de  $\text{Mn}_3\text{O}_4$ . *J. Phys. Chem. Solids* 32 (10), 2429–2437.
- Burns, R.G., 1993. Mineralogical applications of crystal field theory. In: Cambridge Topics in Mineral Physics and Chemistry. Cambridge University Press, New York.
- Chartier, A., D'Arco, P., Dovesi, R., Saunders, V.R., 1999. Ab initio Hartree-Fock investigation of the structural, electronic, and magnetic properties of  $\text{Mn}_3\text{O}_4$ . *Phys. Rev. B* 60 (20), 14042–14048.
- Cornell, R.M., Schwertmann, U., 2003. The Iron Oxides: Structure, Properties, Reactions, Occurrences and Uses. Wiley-VCH, Weinheim.
- Dong, R., Ye, Q., Kuang, L., Lu, X., Zhang, Y., 2013. Enhanced supercapacitor performance of  $\text{Mn}_3\text{O}_4$  nanocrystals by doping transition-metal ions. *ACS Appl. Mater. Interfaces* 5 (19), 9508–9516.
- Feng, X.H., Liu, F., Tan, W.F., Liu, X.W., 2004. Synthesis of birnessite from the oxidation of  $\text{Mn}^{2+}$  by  $\text{O}_2$  in alkali medium: Effects of synthesis conditions. *Clay Clay Miner.* 52 (2), 240–250.
- Gillot, B., El Guendouzi, M., Laarj, M., 2001. Particle size effects on the oxidation-reduction behavior of  $\text{Mn}_3\text{O}_4$  hausmannite. *Mater. Chem. Phys.* 70 (1), 54–60.
- Giovannelli, F., Autret-Lambert, C., Mathieu, C., Chartier, T., Delorme, F., Seron, A., 2012. Synthesis of manganese spinel nanoparticles at room temperature by coprecipitation. *J. Solid State Chem.* 192, 109–112.
- Green, W.J., Stage, B.R., Bratina, B.J., Wagers, S., Preston, A., O'Bryan, K., Shacat, J., Newell, S., 2004. Nickel, copper, zinc and cadmium cycling with manganese in Lake Vanda (Wright Valley, Antarctica). *Aquat. Geochem.* 10 (3), 303–323.
- Hao, X., Zhao, J., Li, Y., Zhao, Y., Ma, D., Li, L., 2011. Mild aqueous synthesis of octahedral  $\text{Mn}_3\text{O}_4$  nanocrystals with varied oxidation states. *Colloids Surf. A Physicochem. Eng. Asp.* 374 (1–3), 42–47.
- Hirai, S., Yagi, S., Seno, A., Fujioka, M., Matsuda, T., 2016. Enhancement of the oxygen evolution reaction in  $\text{Mn}^{3+}$ -based electrocatalysts: correlation between Jahn-Teller distortion and catalytic activity. *RSC Adv.* 6 (3), 2019–2023.
- Huheey, J.E., Keiter, E.A., Keiter, R.L., Medhi, O.K., 1993. Inorganic Chemistry: Principles of Structure and Reactivity. Pearson Education.
- Ilton, E.S., Post, J.E., Heaney, P.J., Ling, F.T., Kerisit, S.N., 2016. XPS determination of Mn oxidation states in Mn (hydro)oxides. *Appl. Surf. Sci.* 366, 475–485.
- Jarosch, D., 1987. Crystal structure refinement and reflectance measurements of hausmannite,  $\text{Mn}_3\text{O}_4$ . *Mineral. Petrol.* 37 (1), 15–23.
- Jha, A., Thapa, R., Chattopadhyay, K.K., 2012. Structural transformation from  $\text{Mn}_3\text{O}_4$  nanorods to nanoparticles and band gap tuning via Zn doping. *Mater. Res. Bull.* 47 (3), 813–819.
- Johnson, K.L., Mccann, C.M., Wilkinson, J.L., Jones, M., Tebo, B.M., West, M., Elgy, C.E., Clarke, C.E., Gowdy, C., Hudson-Edwards, K.A., 2018. Dissolved Mn(III) in water treatment works: Prevalence and significance. *Water Res.* 140, 181–190.
- Julien, C.M., Massot, M., Poinson, C., 2004. Lattice vibrations of manganese oxides: part I. Periodic structures. *Spectrochim. Acta A Mol. Biomol. Spectrosc.* 60 (3), 689–700.
- Kelly, S.D., Hesterberg, D., Ravel, B., 2008. Analysis of soils and minerals using X-ray absorption spectroscopy. In: Ulrey, A.L., Drees, R.L. (Eds.), *Methods of Soil Analysis, Part 5-Mineralogical Methods*. Soil Science Society of America, Wisconsin, pp. 387–463.
- Kim, J.G., Dixon, J.B., Chusuei, C.C., Deng, Y.J., 2002. Oxidation of chromium(III) to (VI) by manganese oxides. *Soil Sci. Soc. Am. J.* 66 (1), 306–315.
- Kim, H., Dixon, J.B., Chusuei, C.C., Deng, Y.J., 2012. Multicomponent effects on the crystal structures and electrochemical properties of spinel-structured  $\text{M}_3\text{O}_4$  ( $M = \text{Fe}, \text{Mn}, \text{Co}$ ) anodes in lithium rechargeable batteries. *Chem. Mater.* 24 (4), 720–725.
- Kirilov, S.A., Aleksandrova, V.S., Lisnycha, T.V., Dzanashvili, D.I., Khainakov, S.A., García, J.R., Visloguzova, N.M., Pendelyuk, O.I., 2009. Oxidation of synthetic hausmannite ( $\text{Mn}_3\text{O}_4$ ) to manganite ( $\text{MnOOH}$ ). *J. Mol. Struct.* 928 (1), 89–94.
- Kohler, T., Armbruster, T., Libowitzky, E., 1997. Hydrogen bonding and Jahn-Teller distortion in groutite,  $\alpha$ - $\text{MnOOH}$ , and manganite,  $\gamma$ - $\text{MnOOH}$ , and their relations to the manganese dioxides ramsdellite and pyrolusite. *J. Solid State Chem.* 133 (2), 486–500.
- Kwon, K.D., Refson, K., Spósito, G., 2009. Zinc surface complexes on birnessite: a density functional theory study. *Geochim. Cosmochim. Acta* 73 (5), 1273–1284.
- Lan, S., Wang, X., Yin, H., Tan, W., Qiu, G., Liu, F., Zhang, J., Feng, X., 2017. Mechanisms of Mn(II) catalytic oxidation on ferrihydrite surfaces and the formation of manganese (oxy)hydroxides. *Geochim. Cosmochim. Acta* 211, 79–96.
- Lefkowitz, J.P., Elzinga, E.J., 2015. Impacts of aqueous Mn(II) on the sorption of Zn(II) by hexagonal birnessite. *Environ. Sci. Technol.* 49 (8), 4886–4893.

- Lide, D.R., Haynes, W.M., 2010. CRC Handbook of Chemistry and Physics. CRC Press, Florida.
- Liu, L., Wang, X., Zhu, M., Ma, J., Zhang, J., Tan, W., Feng, X., Yin, H., Liu, F., 2019. The speciation of Cd in Cd-Fe coprecipitates: does Cd substitute for Fe in goethite structure? *ACS Earth Space Chem.* 3 (10), 2225–2236.
- Manceau, A., Silvester, E., Bartoli, C., Lanson, B., Drits Victor, A., 1997. Structural mechanism of  $\text{Co}^{2+}$  oxidation by the phyllo-manganate buserite. *Am. Mineral.* 1150.
- McKenzie, R., 1970. The reaction of cobalt with manganese dioxide minerals. *Soil Res.* 8 (1), 97–106.
- Nogués, M., Poix, P., 1974. Effet Jahn-Teller coopératif dans le système  $\text{Mn}_3\text{O}_4\text{-Mn}_2\text{SnO}_4$ . *J. Solid State Chem.* 9 (4), 330–335.
- Portier, J., Campet, G., Etourneau, J., Tanguy, B., 1994. A simple model for the estimation of electronegativities of cations in different electronic states and coordinations. *J. Alloy. Compd.* 209 (1–2), 285–289.
- Pozas, R., Rojas, T.C., Ocana, M., Serna, C.J., 2004. The nature of Co in synthetic Co-substituted goethites. *Clay Clay Miner.* 52 (6), 760–766.
- Qin, Z., Xiang, Q., Liu, F., Xiong, J., Koopal, L., Zheng, L., Ginder-Vogel, M., Wang, M., Feng, X., Tan, W., Yin, H., 2017. Local structure of  $\text{Cu}^{2+}$  in Cu-doped hexagonal turbostratic birnessite and  $\text{Cu}^{2+}$  stability under acid treatment. *Chem. Geol.* 466 (S0009254117303984).
- Rabiei, S., Miser, D.E., Lipscomb, J.A., Saoud, K., Gedevisanishvili, S., Rasouli, F., 2005. Conversion of hausmannite ( $\text{Mn}_3\text{O}_4$ ) particles to nano-fibrous manganite ( $\text{MnOOH}$ ) at ambient conditions. *J. Mater. Sci.* 40 (18), 4995–4998.
- Rajeesh Kumar, N.K., Vasylechko, L., Sharma, S., Yadav, C.S., Selvan, R.K., 2021. Understanding the relationship between the local crystal structure and the ferrimagnetic ordering of  $\text{Co}_x\text{Mn}_{3-x}\text{O}_4$  ( $x = 0\text{--}0.5$ ) solid solutions. *J. Alloys Compd.* 853, 157256.
- Ravel, B., Newville, M., 2006. ATHENA and ARTEMIS: Interactive graphical data analysis using IFEFFIT. *Phys. Scr.* 2005 (T115), 1007.
- Rehr, J.J., Albers, R.C., Zabinsky, S.I., 1992. High-order multiple-scattering calculations of x-ray-absorption fine structure. *Phys. Rev. Lett.* 69 (23), 3397–3400.
- Şahin, B., Aydın, R., Cetin, H., 2020. Tuning the morphological, structural, optical and dielectric properties of hausmannite ( $\text{Mn}_3\text{O}_4$ ) films by doping heavy metal lead. *Superlattice. Microst.* 143, 106546.
- Shannon, R., 1976. Revised effective ionic radii and systematic studies of interatomic distances in halides and chalcogenides. *Acta Crystallogr. Sec. A* 32 (5), 751–767.
- Shaughnessy, D.A., Nitsche, H., Booth, C.H., Shuh, D.K., Waychunas, G.A., Wilson, R.E., Gill, H., Cantrell, K.J., Serne, R.J., 2003. Molecular interfacial reactions between Pu (VI) and manganese oxide minerals manganite and hausmannite. *Environ. Sci. Technol.* 37 (15), 3367–3374.
- Sherman, D.M., 1984. The electronic structures of manganese oxide minerals. *Am. Mineral.* 69 (7–8), 788–799.
- Song, B., Cerkez, E.B., Elzinga, E.J., Kim, B., 2020. Effects of Ni incorporation on the reactivity and stability of hausmannite ( $\text{Mn}_3\text{O}_4$ ): Environmental implications for Mn, Ni, and As solubility and cycling. *Chem. Geol.* 558, 119862.
- Spencer, C.D., Schroeder, D., 1974. Mössbauer study of several cobalt spinels using  $\text{Co}^{57}$  and  $\text{Fe}^{57}$ . *Phys. Rev. B* 9 (9), 3658–3665.
- Sukhdev, A., Challa, M., Narayani, L., Manjunatha, A.S., Pasha, M., 2020. Synthesis, phase transformation, and morphology of hausmannite  $\text{Mn}_3\text{O}_4$  nanoparticles: photocatalytic and antibacterial investigations. *Heliyon* 6 (1), e03245.
- Valldor, M., Andersson, M., 2002. The structure of the new compound  $\text{YBaCo}_4\text{O}_7$  with a magnetic feature. *Solid State Sci.* 4 (7), 923–931.
- Wilk, P.A., Shaughnessy, D.A., Wilson, R.E., Nitsche, H., 2005. Interfacial interactions between Np(V) and manganese oxide minerals manganite and hausmannite. *Environ. Sci. Technol.* 39 (8), 2608–2615.
- Xu, H., Xu, S., Wang, H., Yan, H., 2005. Characterization of hausmannite  $\text{Mn}_3\text{O}_4$  thin films by chemical bath deposition. *J. Electrochem. Soc.* 152 (12), C803.
- Yin, H., Liu, F., Feng, X., Liu, M., Tan, W., Qiu, G., 2011.  $\text{Co}^{2+}$ -exchange mechanism of birnessite and its application for the removal of  $\text{Pb}^{2+}$  and As(III). *J. Hazard. Mater.* 196, 318–326.
- Yin, H., Zheng, L., Cui, H., Qiu, G., Liu, F., Feng, X., 2012. Characterization of Ni-rich hexagonal birnessite and its geochemical effects on aqueous  $\text{Pb}^{2+}/\text{Zn}^{2+}$  and As(III). *Geochim. Cosmochim. Acta* 93, 47–62.
- Yin, H., Liu, F., Feng, X., Hu, T., Zheng, L., Qiu, G., Koopal, L.K., Tan, W., 2013. Effects of Fe doping on the structures and properties of hexagonal birnessites - Comparison with Co and Ni doping. *Geochim. Cosmochim. Acta* 117, 1–15.
- Yin, H., Li, H., Wang, Y., Ginder-Vogel, M., Qiu, G., Feng, X., Zheng, L., Liu, F., 2014. Effects of Co and Ni co-doping on the structure and reactivity of hexagonal birnessite. *Chem. Geol.* 381, 10–20.
- Yin, H., Liu, Y., Koopal, L.K., Feng, X., Chu, S., Zhu, M., Liu, F., 2015. High Co-doping promotes the transition of birnessite layer symmetry from orthogonal to hexagonal. *Chem. Geol.* 410, 12–20.
- Yin, H., Sun, J., Yan, X., Yang, X., Feng, X., Tan, W., Qiu, G., Zhang, J., Ginder-Vogel, M., Liu, F., 2020a. Effects of Co(II) ion exchange, Ni(II)- and V(V)-doping on the transformation behaviors of Cr(III) on hexagonal turbostratic birnessite-water interfaces. *Environ. Pollut.* 256, 113462.
- Yin, H., Wu, Y., Hou, J., Yan, X., Li, Z., Zhu, C., Zhang, J., Feng, X., Tan, W., Liu, F., 2020b. Preference of Co over Al for substitution of Fe in goethite ( $\alpha\text{-FeOOH}$ ) structure: Mechanism revealed from EXAFS, XPS, DFT and linear free energy correlation model. *Chem. Geol.* 532, 119378.
- Zhang, F., Zhang, X.G., Hao, L., 2011. Solution synthesis and electrochemical capacitance performance of  $\text{Mn}_3\text{O}_4$  polyhedral nanocrystals via thermolysis of a hydrogen-bonded polymer. *Mater. Chem. Phys.* 126 (3), 853–858.
- Zhao, Y., Li, C., Li, F., Shi, Z., Feng, S., 2011. One-step synthesis of highly water-dispersible  $\text{Mn}_3\text{O}_4$  nanocrystals. *Dalton Trans.* 40 (3), 583–588.
- Zhao, Q., Yan, Z., Chen, C., Chen, J.J.C.R., 2017. Spinel: Controlled preparation, oxygen reduction/evolution reaction application, and beyond. *Chem. Rev.* 117 (15), 10121.